2011

Robustness Analysis For Turbomachinery Stall Flutter

Md Moinul Forhad
University of Central Florida

ROBUSTNESS ANALYSIS FOR TURBOMACHINERY STALL FLUTTER

by

MD MOINUL ISLAM FORHAD
B.Sc. Bangladesh University of Engineering & Technology, 2008

A thesis submitted in partial fulfillment of the requirements
for the degree of Master of Science
in the Department of Mechanical, Materials & Aerospace Engineering
in the College of Engineering & Computer Science
at the University of Central Florida
Orlando, Florida

Summer Term
2011

Major Professor: Yunjun Xu

ABSTRACT

Flutter is an aeroelastic instability phenomenon that can result either in serious damage or complete destruction of a gas turbine blade structure due to high cycle fatigue. Although 90% of potential high cycle fatigue occurrences are uncovered during engine development, the remaining 10% stand for one third of the total engine development costs. Field experience has shown that during the last decades as much as 46% of fighter aircrafts were not mission-capable in certain periods due to high cycle fatigue related mishaps.

To assure a reliable and safe operation, potential for blade flutter must be eliminated from the turbomachinery stages. However, even the most computationally intensive higher order models of today are not able to predict flutter accurately. Moreover, there are uncertainties in the operational environment, and gas turbine parts degrade over time due to fouling, erosion and corrosion resulting in parametric uncertainties. Therefore, it is essential to design engines that are robust with respect to the possible uncertainties. In this thesis, the robustness of an axial compressor blade design is studied with respect to parametric uncertainties through the Mu analysis. The nominal flutter model is adopted from [9]. This model was derived by matching a two dimensional incompressible flow field across the flexible rotor and the rigid stator. The aerodynamic load on the blade is derived via the control volume analysis. For use in the Mu analysis, first the model originally described by a set of partial differential equations is reduced to ordinary differential equations by the Fourier series based collocation method. After that, the nominal model is obtained by linearizing the achieved non-linear ordinary differential equations. The uncertainties coming from the modeling assumptions and imperfectly known parameters and coefficients are all modeled as parametric uncertainties through the Monte Carlo simulation. As

compared with other robustness analysis tools, such as H_{inf}, the Mu analysis is less conservative and can handle both structured and unstructured perturbations.

Finally, Genetic Algorithm is used as an optimization tool to find ideal parameters that will ensure best performance in terms of damping out flutter. Simulation results show that the procedure described in this thesis can be effective in studying the flutter stability margin and can be used to guide the gas turbine blade design.

ACKNOWLEDGMENTS

First of all, I would like to extend sincere appreciations to my advisor Dr. Yunjun Xu for his immense academic insight, patient attitude in answering my questions and continuous support to my MS study and research. I could not finish this research and thesis without his guidance.

Beside my advisor, I would like to thank the of my thesis committee members: Dr. Jayanta Kapat and Dr. Seetha Raghavan, for their insightful comments, correction, and help on my thesis.

I am very thankful to all of my colleagues in the Dynamics and Controls Lab for wonderful friendships, which I have enjoyed throughout my studies here.

Finally, I would like to thank my family and my friends, for standing behind me and supporting me spiritually throughout my life.

TABLE OF CONTENTS

LIST OF FIGURES

LIST OF TABLES

NOMENCLATURE

A_t : Throttle parameter

B : Greitzer B parameter

c : Rotor chord length

c_s : Stator chord length

D : Blade mass

F_l : Lift force on the blade due to fluid flow

I_{ea} : Moment of inertia of the blade about elastic axis

$\hat{i}$: Unit vector in the axial direction

$\hat{j}$: Unit vector in the tangential direction

L_c : Compressor duct length

L_I : Inlet duct length

L_r : Rotor pressure loss

$L_{r,\,qs}$: Quasi-steady rotor total pressure loss

$L_{s,\,qs}$: Quasi-steady stator total pressure loss

L_{r1} : Coefficient of the empirical rotor loss function

L_{r2} : Coefficient of the empirical rotor loss function

L_{r3} : Coefficient of the empirical rotor loss function

L_{s1} : Coefficient of the empirical stator loss function

L_{s2} : Coefficient of the empirical stator loss function

L_{s3} : Coefficient of the empirical stator loss function

L_s : Stator pressure loss

M : Aerodynamic moment about the elastic axis

N_B : Number of blades

p_{atm} : Atmospheric pressure non-dimensionalized by ρU_T^2

Q_b : Frequency of the pure bending mode

Q_t : Frequency of the pure torsion mode

q : Bending displacement of the blade

t : Non-dimensional time

U_T : Tip speed

v : Non-dimensional tangential velocity, C_θ / U_T

x : Axial coordinate

X : States in the non-linear and linear models

α : Torsional displacement of the blade

β_r : Trailing edge metal angle of the rotor

β_{zr} : Zero-incidence angle of the rotor leading edge

β_{zs} : Zero-incidence angle of the stator leading edge

γ_r : Stagger angle of the rotor

γ_s : Stagger angle of the stator

ε : Rotational inertia divided by chord

Φ : Non-dimensional mass Flow, C_x / U_T

$\tilde{\phi}$: Perturbation axial velocity

Ψ : Non-dimensional pressure, $P/\rho U_T^2$

Ψ_P : Non-dimensional plenum Pressure, $P_p/\rho U_T^2$

$\tilde{\psi}$: Perturbation pressure

τ_r : Time scale for the rotor loss

τ_s : Time scale for the stator loss

ξ_{ea} : Position of the elastic axis of the blade from the leading edge divided by the blade-chord

ξ_{cg} : Position of the center of gravity of the blade from the leading edge divided by the blade-chord

ξ_{cp} : Position of the center of pressure of the blade from the leading edge divided by the blade-chord

ς_b : Structural damping of the bending mode

ς_t : Structural damping of the torsion mode

δ_1 : Coefficient of the empirical rotor deviation function

δ_2 : Coefficient of the empirical rotor deviation function

Subscripts:

1 : Inlet of the actuator disk

2 : Exit of the rotor, inlet of the stator

3 : Exit of the stator

le : Leading edge

rel : In the rotor (rotating) reference frame

r : Rotor

s : Stator

te : Trailing edge

CHAPTER ONE: INTRODUCTION

Background of Turbomachinery Instabilities

Compression system such as gas turbines can exhibit several types of instabilities: combustion instabilities, aeroelastic instabilities such as flutter and aerodynamic flow instabilities such as rotating stall and surge. The aerodynamic instabilities limit the flow range in which the compressor can operate. At high mass flow rate, the operation of turbo-compressors is limited by choking while at low mass flows, operation of turbomachines is restricted by the onset of two other instabilities known as surge and rotating stall. Apart from the operability, the performance and efficiency of the compressors are also limited by surge and rotating stall. The aerodynamic instabilities may also lead to heating of the blades and to an increase in the exit temperature of the compressor [1-3].

Flutter in Turbomachinery

Gas turbines and other turbomachines constitute rotating blades and guiding vanes. Out of the whole gas turbine, the compression system is more susceptible to aerodynamic and aeroelastic instabilities. The current research focuses on analyzing the robustness of turbomachines in terms of flutter. As compared to stationary vanes, rotating blades are more susceptible to fluttering, and the risk of blade flutter in turbine applications has received attention due to increasing operational demands and aggressive design requirements recently. For example high lift and low mass designs in aero-engines [5]. To assure reliability and safety of jet propulsion, the potential for blade flutter must be eliminated from the turbomachinery stages.

From both experimental and theoretical studies [5-6], it is found that flutter is caused primarily by the interaction of the turbomachinery blade motion with incoming flow fields. As a result, unsteady aerodynamic forces and moments are generated on the blade surface. When the

aerodynamic damping resulted from these aerodynamic forces and moments is negative and exceeds the available blade structural damping, a marked increase in blade vibratory response will occur. When the vibration levels exceed the material endurance limits, blade flutter failure soon results.

Motivation for the Research

The aeroelastic instability phenomenon of flutter can result either in serious damage or complete destruction of a gas turbine blade structure due to high cycle fatigue. Although 90% of potential high cycle fatigue occurrences are uncovered during engine development, the remaining 10% stand for one third of the total engine development costs [4]. Field experience has shown that during the last decades as much as 46% of fighter aircrafts were not mission-capable in certain periods due to high cycle fatigue related mishaps.

Significant advances in the understanding of blade flutter have been achieved through numerous experimental and theoretical investigations. Much attention has been focused on compressors due to their well documented predisposition to blade flutter under certain operation regimes [5].

Although the advances in understanding the blade flutter have been quite significant, the current models for turbomachinery flutter are normally computationally intensive, and it is difficult to ensure high fidelity. Also, the number of states is prohibitively high such that a systematic analysis of the flutter phenomenon is not easy to achieve [6]. Reduced order models have been constructed to obtain a computationally more tractable system [7]. But these models suffer from either one or several of the following limitations: (1) not including the vibration mode shape, (2) typically cannot capture the flows over different geometries and Mach numbers, (3) only valid for small perturbations about a steady state.

Considering various shortcomings of the models resulting in lack of proper tools to predict flutter accurately, to ensure a safe operation it is therefore important to study the robustness of a turbomachinery blade design in the presence of uncertainties. In this thesis, the robustness of an axial compression system is studied with respect to parametric uncertainties.

This thesis also demonstrates an application of Genetic Algorithm as an optimization tool to find ideal parameters that will ensure best performance in terms of damping out flutter. Simulation results show that the procedure described in this thesis can be effective in studying the flutter stability margin and can be used to guide the gas turbine blade design.

Research Advantages

The research outlined in this thesis focuses on: (1) studying the robustness of an axial compression system in terms of flutter, under the presence of different uncertainties (2) finding the best parameter set that can improve the performance in terms of flutter.

The necessity of robustness study for these machines is the result of the fact that robust design must be ensured because of the following three major reasons: (1) the most computationally expensive flutter models are not able to predict flutter accurately (2) some of the parameters of the machine are not perfectly known and their values change over time as a result of degradation due to fouling, erosion, corrosion etc (3) there are uncertainties in the operating environment of the machines.

The major technical challenges addressed in this thesis are shown as follows:

First, the original model is organized in a form which is easy to use for control-oriented studies.

Second, in order to obtain a linear model for the subsequent Mu analysis, the original PDE model is reduced to a non-linear ODE model in state space form by means of Fourier series

based collocation method. The non-linear model is then linearized about the equilibrium points, which are found with the help of non-linear solvers, using small perturbation method.

Third, Mu analysis is done for robustness study of the system under the presence of the uncertainties and using the linear model achieved in the previous step. Also, Genetic Algorithm is applied to find the best parameter set that can optimize the performance in terms of flutter.

Thesis Outline

The analytical model used in this thesis as the nominal model of the system is described in details in Chapter 2. This model is adopted from [9] and reorganized in this thesis in a form which is easy to use for control-oriented studies.

While a linear model is needed for the robustness analysis using the Mu tool, the original model, which describes the physical phenomenon of fluid-solid interaction in the axial compression system, is in PDE form. As the first step of achieving the linear model, the original PDE model is reduced to a non-linear ODE model by means of a Fourier series based collocation method. In Chapter 3 of the thesis, the procedure for achieving this non-linear model is shown in details.

The non-linear model is linearized about the equilibrium points in the next step. The procedure for obtaining the linear model by small perturbation method is discussed in Chapter 4. This chapter also includes a description of linear stability analysis done in this thesis.

In Chapter 5 of the thesis, the procedure for quantification of uncertainty bounds on the linear model via Monte Carlo simulation is shown.

Chapter 6 describes the formulation of the problem for Mu analysis and the simulation results.

With a view to optimizing the performance in terms of flutter, Genetic algorithm is used

as the tool to search the ideal parameters. The results are shown in Chapter 7.

Chapter 8 is the summary and conclusion of this thesis work.

CHAPTER TWO: FLUTTER MODEL

The compression system as shown in Figure 1, composed of an inlet duct, an axial compressor stage of flexible rotors and rigid stators, a plenum chamber, and a throttle, is considered. The compressor pumps the flow into the plenum, which exhausts through a throttle.

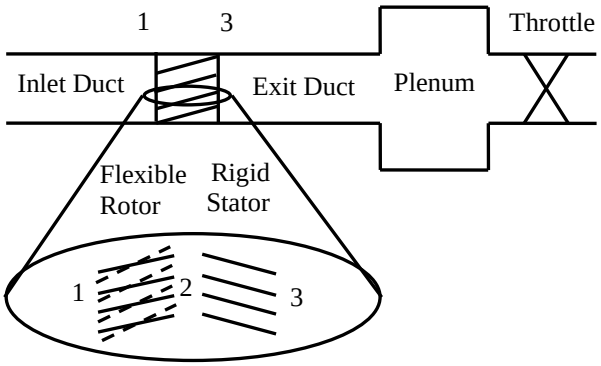

Figure 1: Compression system schematic

The equations of the flutter model used here are adopted from [8-9]. A high hub-to-tip ratio is assumed in deriving the model such that the flow can be treated as two-dimensional, with the variations considered in the axial and circumferential directions only. The compressor ducts are assumed to be long enough so that there is no non-axisymmetric pressure field interaction with the end terminations. The flow external to the blade rows is considered to be inviscid. Compressibility effects are neglected assuming low Mach numbers in the compressor and ducts. In the plenum, where the compressibility effects are important, density changes are related to the pressure changes through an isentropic relation [10]. Losses are introduced into the rotor and stator stages through the empirical total pressure loss relations. The flexible rotor blades are represented by a simple two dimensional, two degrees of freedom model, which is done using a typical section with an inertial and aerodynamic coupling between twist and plunge. A control

volume analysis is used to couple the aerodynamics and structural dynamics, which provides the effect of the aeroelastic phenomenon. The deformed blade passages are defined and analyzed as a deformable control volume across flexible rotors coupled with a structural model [8-9].

In this thesis, the equations presented in [8-9] have been reorganized in a form that can be easily used in the Mu robustness analysis later. Detailed discussions on the model can be found in [8-14].

Inlet and Exit Duct

The annular inlet and exit ducts are assumed to have a constant height, and the flow is assumed to be incompressible. In the inlet duct, only the potential flow perturbations can be created by the compressor and these decay upstream. Hence, for an axisymmetric meanflow, the linearized relation between the non-axisymmetric static pressure and the axial velocity perturbations at the inlet (station 1), as given in [11], is

$$\tilde{\psi}_1 = -\mathrm{Re}\sum_{n=1}^{N}\left[\frac{1}{n}\frac{\partial\hat{\tilde{\phi}}_{1_n}}{\partial t}+\bar{\phi}_1\ \ \hat{\tilde{\phi}}_{1_n}(t)\right]e^{in\theta} \tag{1}$$

where $\bar{\phi}_1 = (1/2\pi)\int_0^{2\pi}\Phi_1(t,\theta)d\theta$, and $\Phi_1 = \bar{\phi}_1 + \tilde{\phi}_1$. $\hat{\tilde{\phi}}_{1_n}$ is the nth harmonic component of non-axisymmetric axial velocity perturbation at station 1, while "Re" denotes the real part of the complex term in Eq. (1) and N is the highest number of harmonics used to describe the inlet axial velocity Φ_1.

In the exit duct, the only disturbances considered are the decaying potential field downstream and the vorticity associated with the variation in the compressor loading around the annulus. The analysis is simplified by the assumption that the stators fix the exit flow angle to be axial (i.e. no deviation effects). This produces the following relation between the non-

axisymmetric pressure distribution at the exit of the compressor (Station 3) and the flow perturbations [11].

$$\tilde{\psi}_3 = \mathrm{Re}\sum_{n=1}^{N}\left[\frac{1}{n}\frac{\partial\hat{\tilde{\phi}}_{3n}}{\partial t}\right]e^{in\theta} \tag{2}$$

$\hat{\tilde{\phi}}_{3n}$ is the n[th] harmonic component of non-axisymmetric axial velocity perturbation at station 3. Equations (1) and (2) are used together with Equations (32) and (36), which are shown later in this thesis, to calculate the pressures at stations 1 and 3.

Plenum and Throttle

As shown in [4], the conservation of the axial momentum in the inlet and exit ducts, and the conservation of the mass in an isentropic plenum results in the following equations:

$$\frac{1}{2\pi}\int_0^{2\pi}\left[(\Psi_3 - \Psi_1) - \Psi_P = L_c\frac{\partial\Phi_1}{\partial t}\right]d\theta \tag{3}$$

and

$$\frac{1}{2\pi}\int_0^{2\pi}\left[\Phi_1 - A_t\sqrt{2\Psi_P} = 4B^2 L_c\frac{\partial\Psi_P}{\partial t}\right]d\theta \tag{4}$$

Equations (3) and (4) are related to two states: Φ_1 and Ψ_P.

Blade Dynamics

As described by Dowel [15] and Gysling and Myers [10], the structural dynamics of the blade is modeled considering a typical section with the inertial and aerodynamic coupling between the twist and plunge motions. The lift force is assumed to act at the center of pressure, which is assumed constant. The two modes considered here are the twist and plunge as illustrated in Figure 2.

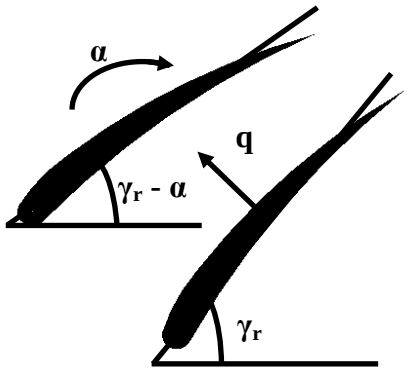

Figure 2: Blade deflection indicating the twist α and plunge q (modified based on [9])

The plunge equation is described by

$$\left(\frac{\partial}{\partial t}-\frac{\partial}{\partial \theta}\right)^2 q+\left(\xi_{ea}-\xi_{cp}\right)c\left(\frac{\partial}{\partial t}-\frac{\partial}{\partial \theta}\right)^2 \alpha$$
$$+2\varsigma_b Q_b\left(\frac{\partial}{\partial t}-\frac{\partial}{\partial \theta}\right)q+Q_b^2 q=\frac{F_l}{D} \tag{5}$$

while the twist equation is

$$\left(\frac{\partial}{\partial t}-\frac{\partial}{\partial \theta}\right)^2 \alpha+\frac{\left(\xi_{ea}-\xi_{cg}\right)cD}{I_{ea}}\left(\frac{\partial}{\partial t}-\frac{\partial}{\partial \theta}\right)^2 q$$
$$+2\varsigma_t Q_t\left(\frac{\partial}{\partial t}-\frac{\partial}{\partial \theta}\right)\alpha+Q_t^2\alpha=\frac{M}{I_{ea}} \tag{6}$$

where the moment of inertia I_{ea} can be calculated by

$$I_{ea}=D\left(\xi_{ea}-\xi_{cg}\right)^2 c^2+Dc^2\varepsilon^2 \tag{7}$$

The lift force on the blade F_l in Eq. (5) is calculated by

$$F_l=\frac{F_\theta\cos\left(\gamma_r-\alpha\right)-F_x\sin\left(\gamma_r-\alpha\right)}{2} \tag{8}$$

where F_x and F_θ are axial and circumferential components of the force on the blade $\vec{F}=F_x\hat{\mathrm{i}}+F_\theta\hat{\mathrm{j}}$. F_x and F_θ can be calculated through the control volume analysis across two

adjacent blades to be describe in the next section. The moment about the elastic axis in Eq. (6) is given by

$$M = F_l\left(\xi_{ea} - \xi_{cp}\right)c \tag{9}$$

There are four state variables in Equations (5) and (6): α, $\dot{\alpha}$, q and $\dot{q}$.

Control Volume Analysis

The two components of the force on the blade, F_x and F_θ, can be calculated based on the conservation of the momentum equation across the rotor described by

$$\begin{aligned}&\left(\frac{\partial}{\partial t} - \frac{\partial}{\partial \theta}\right)\left(\vec{v}\frac{\partial V}{\partial \theta}\right) + \left[\vec{v}_{le}\left(\vec{v}_{rel,le}\cdot\vec{n}_{le}\right) + p_{le}\vec{n}_{le}\right]\frac{\partial s_{le}}{\partial \theta} \\ &+\left[\vec{v}_{te}\left(\vec{v}_{rel,te}\cdot\vec{n}_{te}\right) + p_{te}\vec{n}_{te}\right]\frac{\partial s_{te}}{\partial \theta} = -\frac{\partial \vec{F}}{\partial \theta}\end{aligned} \tag{10}$$

where

$$\frac{\partial V}{\partial \theta} = c\cos(\gamma_r - \alpha)\frac{1}{2}\left(\frac{\partial s_{le}}{\partial \theta} + \frac{\partial s_{te}}{\partial \theta}\right) \tag{11}$$

Force exerted on the blade by the fluid is found by

$$\vec{F} = \int_{\theta_B - \pi/N_B}^{\theta_B + \pi/N_B}\left[\partial \vec{F} / \partial \theta\right] d\theta \tag{12}$$

where θ_B is the blade angular position , which is constant for a blade with respect to a fixed reference.

The two path lengths along the leading and trailing edges can be calculated by

$$\frac{\partial s_{le}}{\partial \theta} = \sqrt{\left(\frac{\partial x_{le}}{\partial \theta}\right)^2 + \left(\frac{\partial \theta_{le}}{\partial \theta}\right)^2} \tag{13}$$

and

$$\frac{\partial s_{te}}{\partial \theta} = \sqrt{\left(\frac{\partial x_{te}}{\partial \theta}\right)^2 + \left(\frac{\partial \theta_{te}}{\partial \theta}\right)^2} \tag{14}$$

respectively. The axial and circumferential coordinates of the leading and trailing edges are given by

$$x_{le} = -q\sin(\gamma_r) - \xi_{ea} c\cos(\gamma_r - \alpha) \tag{15}$$

$$\theta_{le} = \theta + q\cos(\gamma_r) - \xi_{ea} c\,\mathrm{s}in(\gamma_r - \alpha) \tag{16}$$

$$x_{te} = -q\sin(\gamma_r) + (1-\xi_{ea}) c\cos(\gamma_r - \alpha) \tag{17}$$

$$\theta_{te} = \theta + q\cos(\gamma_r) + (1-\xi_{ea}) c\,\mathrm{s}in(\gamma_r - \alpha) \tag{18}$$

The two normal vectors at the blade leading and trailing edges used in Eq. (10) are found as

$$\vec{n}_{le} = -\cos(\beta_{le})\hat{\mathrm{i}} + \sin(\beta_{le})\hat{\mathrm{j}} \tag{19}$$

$$\vec{n}_{te} = \cos(\beta_{te})\hat{\mathrm{i}} - \sin(\beta_{te})\hat{\mathrm{j}} \tag{20}$$

The relative velocities between the flow and the two edges of the blade used in Eq. (10), $\vec{v}_{rel,le}$ and $\vec{v}_{rel,te}$, are given by

$$\vec{v}_{rel,le} = \left(\Phi_1\hat{\mathrm{i}} + v_1\hat{\mathrm{j}}\right) - \left(\frac{\partial}{\partial t} - \frac{\partial}{\partial \theta}\right)\left(x_{le}\hat{\mathrm{i}} + \theta_{le}\hat{\mathrm{j}}\right) \tag{21}$$

and

$$\vec{v}_{rel,te} = \left(\Phi_2\hat{\mathrm{i}} + v_2\hat{\mathrm{j}}\right) - \left(\frac{\partial}{\partial t} - \frac{\partial}{\partial \theta}\right)\left(x_{te}\hat{\mathrm{i}} + \theta_{te}\hat{\mathrm{j}}\right) \tag{22}$$

The axial component of the velocity at the rotor leading edge (station 1) Φ_1 is found from Eq. (3) while the circumferential component v_1 is calculated by the following assumption as suggested by Moore and Greitzer [12].

$$\frac{\partial v_1}{\partial \theta} = -\tilde{\phi}_1 \tag{23}$$

The axial and circumferential velocities at the trailing edge of the rotor (station 2), Φ_2 and v_2, can be found from the conservation of mass equation together with an assumption on flow kinematics. The conservation of mass equation is expressed as

$$\left(\frac{\partial}{\partial t} - \frac{\partial}{\partial \theta}\right)\frac{\partial V}{\partial \theta} + \left(\vec{v}_{rel,le} \cdot \vec{n}_{le}\right)\frac{\partial s_{le}}{\partial \theta} + \left(\vec{v}_{rel,te} \cdot \vec{n}_{te}\right)\frac{\partial s_{te}}{\partial \theta} = 0 \tag{24}$$

The kinematic constraint on the flow is based on the assumption that the fluid exits the blade with a certain deviation angle described by an empirical relation. Following is the equation of kinematic constraint on the flow.

$$v_2 - \left(\frac{\partial}{\partial t} - \frac{\partial}{\partial \theta}\right)\theta_{te} = \left[\Phi_2 - \left(\frac{\partial}{\partial t} - \frac{\partial}{\partial \theta}\right)x_{te}\right]\tan\left(\beta_r - \alpha + \delta\right) \tag{25}$$

where the flow deviation angle at the exit of the rotor, δ, is related to the incidence angle by the following relation.

$$\delta = \delta_1 \alpha_{inc,r} + \delta_2 \tag{26}$$

The rotor incidence angle $\alpha_{inc,r}$ is given by

$$\alpha_{inc,r} = \tan^{-1}\left(\frac{\vec{v}_{rel,le} \cdot \hat{\mathrm{j}}}{\vec{v}_{rel,le} \cdot \hat{\mathrm{i}}}\right) - \beta_{zr} + \alpha \tag{27}$$

The velocity within the control volume, $\vec{v}$ in Eq. (10), is approximated by the mean value of the leading and trailing edge flow velocities as

$$\vec{v} = \frac{1}{2}\left(\vec{v}_{le} + \vec{v}_{te}\right) \tag{28}$$

where

$$\vec{v}_{le} = \Phi_1 \hat{\mathrm{i}} + (1+v_1)\hat{\mathrm{j}} \tag{29}$$

$$\vec{v}_{te} = \Phi_2 \hat{\mathrm{i}} + (1+v_2)\hat{\mathrm{j}} \tag{30}$$

The axisymmetric pressure at the leading edge $\bar{\Psi}_1$ can be calculated by the unsteady Bernoulli's equation [16]

$$p_{atm} - \bar{\Psi}_1 = \frac{1}{2}\left(\Phi_1^2 + v_1^2\right) + L_I \frac{\partial \Phi_1}{\partial t} \tag{31}$$

Thus the expression for p_{le} in Eq. (10), which is essentially the pressure at station 1, Ψ_1, is given by

$$p_{le} = \Psi_1 = \bar{\Psi}_1 + \tilde{\psi}_1 = p_{atm} - \frac{1}{2}\left(\Phi_1^2 + v_1^2\right) + \tilde{\psi}_1 \tag{32}$$

The trailing edge pressure p_{te} used in Eq. (10) can be calculated from the conservation of energy, when the force term in the equation is substituted by the LHS of the conservation of momentum equation. The conservation of energy across the deforming blade passage is given by

$$\begin{aligned} &\left(\frac{\partial}{\partial t} - \frac{\partial}{\partial \theta}\right)\frac{1}{2}v^2 \frac{\partial V}{\partial \theta} + \left(p_{le} + \frac{1}{2}v_{le}{}^2 - L_r\right)\left(\vec{v}_{rel,le} \cdot \vec{n}_{le}\right)\frac{\partial s_{le}}{\partial \theta} \\ &+ \left(p_{te} + \frac{1}{2}v_{te}{}^2\right)\left(\vec{v}_{rel,te} \cdot \vec{n}_{te}\right)\frac{\partial s_{te}}{\partial \theta} = -\frac{\partial \vec{F}}{\partial \theta} \cdot \vec{v}_{cv} \end{aligned} \tag{33}$$

where L_r represents a loss in the leading edge total pressure to account for non-conservative processes, which is governed by Eq. (37) shown in the next section. The velocity of the control volume is given by

$$\vec{v}_{cv} = \left(\frac{\partial}{\partial t} - \frac{\partial}{\partial \theta}\right)\left(\frac{x_{le} + x_{te}}{2}\hat{\mathrm{i}} + \frac{\theta_{le} + \theta_{le}}{2}\hat{\mathrm{j}}\right) + \hat{\mathrm{j}} \tag{34}$$

Analysis for the Stator

The stator is modeled as a rigid blade row, and the conservation of mass across the stator can be expressed as

$$\Phi_2 = \Phi_3 \tag{35}$$

Using the unsteady Bernoulli's equation [10], the following relation is found to govern the pressure rise across the stator

$$(\Psi_{t,3} - \Psi_{t,2}) = \frac{c_s}{\cos(\gamma_s)} \frac{\partial \Phi_2}{\partial \tau} - L_s \tag{36}$$

where L_s represents a loss in the total pressure across the stator, which is governed by Eq. (38) to be shown in the next section. $\Psi_{2,t}$ is the total pressure at the trailing edge of the rotor, while $\Psi_{3,t}$ is the total pressure at the trailing edge of the stator.

Rotor and Stator Losses

The total pressure losses across the rotor and stator disks are assumed to lag their quasi-static values. A simple one dimensional lag equation is used in each case [5].

$$\tau_r \left(\frac{\partial}{\partial t} - \frac{\partial}{\partial \theta} \right) L_r = -\left(L_r - L_{r,qs} \right) \tag{37}$$

$$\tau_s \left(\frac{\partial}{\partial t} - \frac{\partial}{\partial \theta} \right) L_s = -\left(L_s - L_{s,qs} \right) \tag{38}$$

The quasi-static losses $L_{r,qs}$ and $L_{s,qs}$ are assumed to be functions of incidence angle,

$$L_{r,qs} = L_{r1} \alpha_{inc,r}^2 + L_{r2} \alpha_{inc,r} + L_{r3} \tag{39}$$

$$L_{s,qs} = L_{s1} \alpha_{inc,s}^2 + L_{s2} \alpha_{inc,s} + L_{s3} \tag{40}$$

The incidence angle on the rotor is defined in Eq. (27). The incidence angle on the stator is given by

$$\alpha_{inc,s} = -\tan^{-1}\left(\frac{v_2}{\phi_2}\right) - \beta_{zs} \tag{41}$$

Equation (37) and (38) result in two states in the model: L_r and L_s.

CHAPTER THREE: NONLINEAR MODEL VIA FOURIER SERIES BASED COLLOCATION METHOD

Generation of Non-linear Model

To be used in the stability and robustness analysis, the PDE model described in the above section is reduced to an ODE form through the Fourier series based collocation approach following the steps described in [17].

The state variables Φ_1, α, q, L_r and L_s in the model are approximated in terms of the Fourier series as shown below.

$$\Phi_1 = \sum_{n=0}^{N}\left[\varphi_n(t)\cos(n\theta) + \hat{\varphi}_n(t)\sin(n\theta)\right] \tag{42}$$

$$\alpha = \sum_{n=0}^{N}\left[a_n(t)\cos(n\theta) + \hat{a}_n(t)\sin(n\theta)\right] \tag{43}$$

$$q = \sum_{n=0}^{N}\left[b_n(t)\cos(n\theta) + \hat{b}_n(t)\sin(n\theta)\right] \tag{44}$$

$$L_r = \sum_{n=0}^{N}\left[lr_n(t)\cos(n\theta) + \hat{lr}_n(t)\sin(n\theta)\right] \tag{45}$$

$$L_s = \sum_{n=0}^{N}\left[ls_n(t)\cos(n\theta) + \hat{ls}_n(t)\sin(n\theta)\right] \tag{46}$$

in which N is the highest number of harmonics used in the series.

Plenum pressure Ψ_p is assumed to be spatially uniform and hence approximated by a time dependent term only.

$$\Psi_p = \psi_0(t) \tag{47}$$

The unknown variables in the original PDEs are then substituted by the approximation and the residual functions are obtained at the collocation points. In this thesis, the two boundary points of integration and their midpoint are used as the collocation points. A set of ODEs is then obtained by forcing the residual functions to be zero at the collocation points. For brevity, Eq. (37), the rotor loss equation, is used as an example to demonstrate the basic procedure.

$$\tau_r \left(\frac{\partial}{\partial t} - \frac{\partial}{\partial \theta} \right) L_r = -\left(L_r - L_{r,qs} \right) \tag{48}$$

If $N = 1$, the unknown variable rotor loss L_r is approximated by

$$L_r = lr_0(t) + lr_1(t)\cos(\theta) + \hat{lr}_1(t)\sin(\theta) \tag{49}$$

Now substituting L_r in Eq. (48) by the approximation in Eq. (49), following residual equation can be obtained at $\theta = \theta_i$, where $i = 1, 2, 3$.

$$\begin{aligned} &\tau_r \left(\frac{dlr_0(t)}{dt} + \frac{dlr_1(t)}{dt}\cos\theta + \frac{d\hat{lr}_1(t)}{dt}\sin\theta + lr_1(t)\sin\theta - \hat{lr}_1(t)\cos\theta \right) \\ &= -\left(lr_0(t) + lr_1(t)\cos\theta + \hat{lr}_1(t)\sin\theta - L_{r,qs} \right) \end{aligned} \tag{50}$$

The residual equation can be reorganized to obtain a state space representation.

Comparing the simulations with different number of harmonics in the Fourier series approximation, it is found that a series approximation with only zeroth and first order harmonic is sufficient to capture the system dynamics. Following are the 22 states in the reduced order non-linear model:

Variables	States
Φ_1	$\varphi_0, \varphi_1, \hat{\varphi}_1$
Ψ_p	ψ_0
α	$a_0, a_1, \hat{a}_1, \dot{a}_0, \dot{a}_1, \dot{\hat{a}}_1$
q	$b_0, b_1, \hat{b}_1, \dot{b}_0, \dot{b}_1, \dot{\hat{b}}_1$
L_r	$Ir_0, lr_1, \hat{lr}_1$
L_s	$ls_0, ls_1, \hat{ls}_1$

The nonlinear model of the whole compression system in terms of the 22 state variables are then organized in the form of

$$\left[\dot{X}\right]_{22\times1} = [A]_{22\times22}[X]_{22\times1} + [B]_{22\times22}\left[\sqrt{X}\right]_{22\times1} + [f(X,p)]_{22\times1} \tag{51}$$

where $f(X,p)$ is a function of the states, X, and parameter vector p. Matrices $[A]$ and $[B]$ are found to be constant for each operating point; $[A][X]$ denotes the linear part of the model. For the model achieved here, matrix $[B]$ has only one non-zero entry, as the governing equation of the plenum pressure is the only equation in the model with a square root term. Non-linearity of the system comes mainly from the part $f(X,p)$.

Non-linear Simulation Results

The non-linear model achieved by applying the Fourier series based collocation method, as described above, is then simulated using the Runge-Kutta method for solving the Ordinary Differential Equations. Results obtained from the simulations are presented here in Figures 3 to 6.

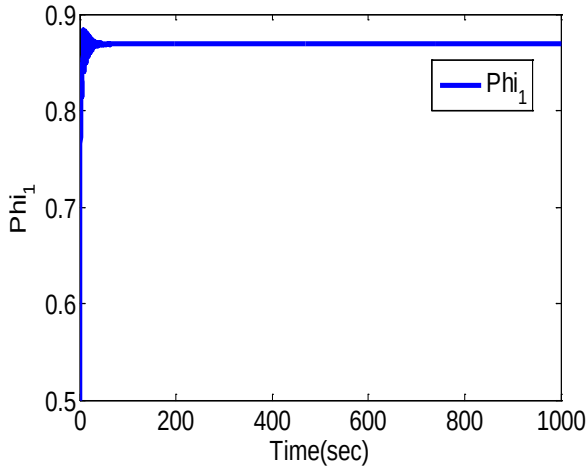

Figure 3: Non-linear simulation results for the non-dimensional mass flow

Figure 3 above shows the simulation results obtained for the non-dimensional mass flow rate. As can be seen in the figure, the mass flow has initial transient, which then achieves the steady-state condition with time.

Presented below in Figure 4 are the simulation results for the non-dimensional plenum pressure. Like the non-dimensional mass flow rate, some initial transients are seen in the plenum pressure, which then reaches the steady-state value with time.

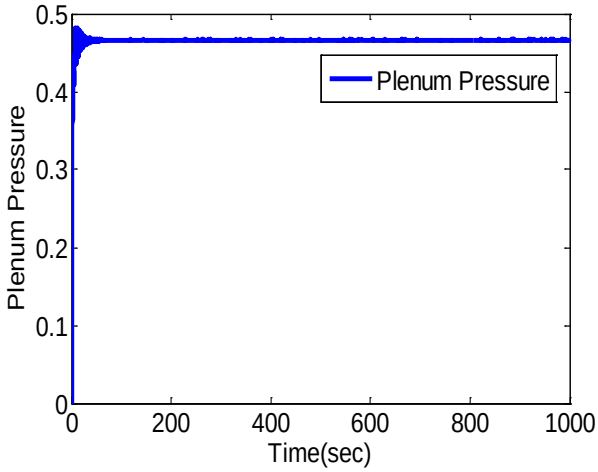

Figure 4: Non-linear simulation results for the non-dimensional plenum pressure

The non-linear simulation results for the bending and twist displacements of the blades are presented in Figure 5, and the simulations results for the rotor and stator losses are presented in Figure 6.

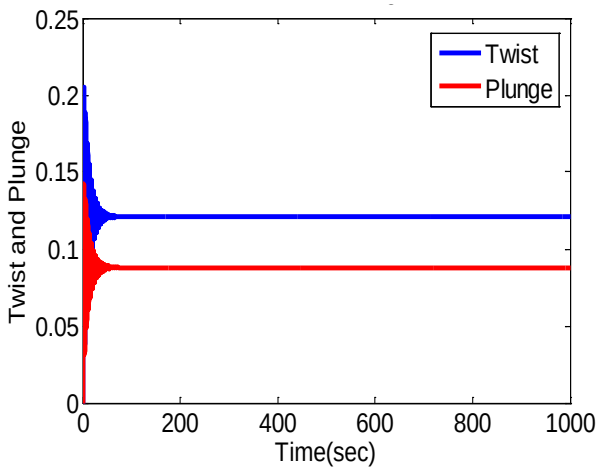

Figure 5: Non-linear simulation results for the non-dimensional twist and bending displacements

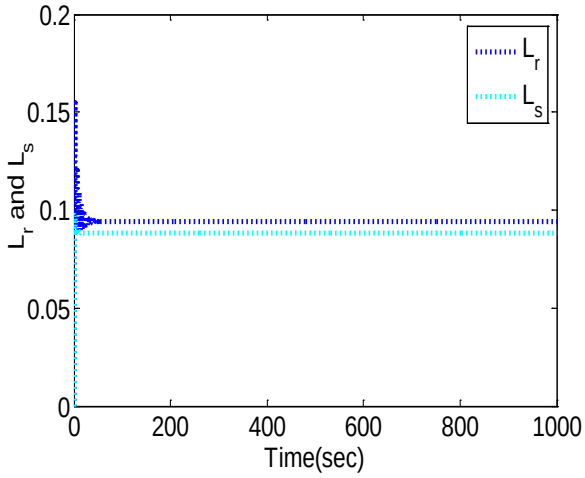

Figure 6: Non-linear simulation results for the rotor and stator losses

CHAPTER FOUR: LINEARIZATION AND STABILITY ANALYSIS

First the equilibrium point of the system (Eq. 51) is found for a throttle parameter (A_t) setting. Then the non-linear model is linearized about the equilibrium point X_{eq} by means of the small perturbation theory. First the partial derivatives of $f(X, p)$ with respect to all the state variables X are found numerically, by using a five point stencil formula. For the model achieved here, matrix $[B]$ has only one non-zero entry, as explained in the previous chapter. Hence, all the partial derivatives of the second term in Eq. 51 can be found analytically. Finally, the Taylor series expansion is utilized to obtain the linearized function for the original non-linear function. All the three matrices combined together, the linearized perturbation model is obtained in the form of $\left[\Delta \dot{X}\right]_{22\times1} = [Z]_{22\times22}[\Delta X]_{22\times1}$, where $X = X_{eq} + \Delta X$.

The eigenvalues of the linear model are calculated to study the stability of the system. The eigenvalues of the linear system obtained for a throttle parameter value of 0.7 is shown in Figure 7.

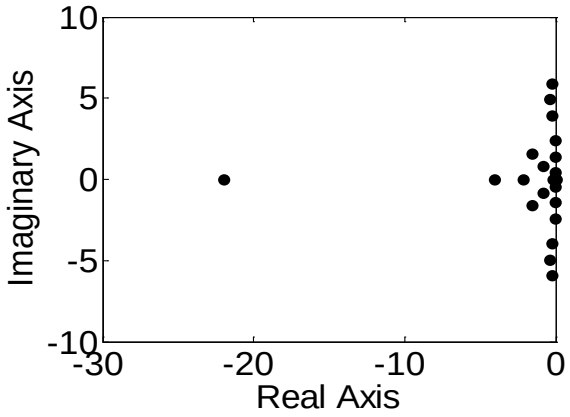

Figure 7: Eigenvalues of the linear system for a throttle parameter value of 0.7

Using the similar procedure, linear models are obtained for other settings of the throttle parameter, and linear stability analysis done. The eigenvalues of the linear model obtained for a throttle parameter value of 0.8 is presented in Figure 8.

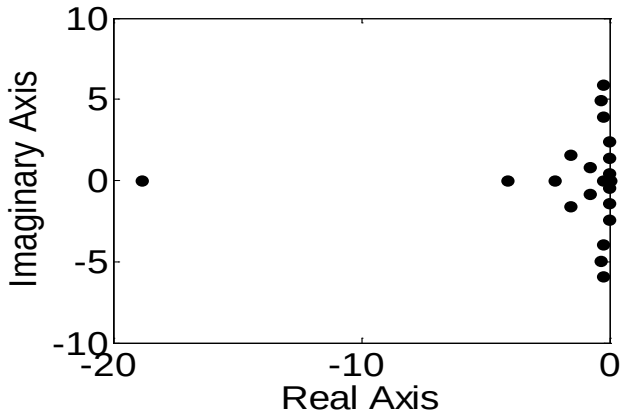

Figure 8: Eigenvalues of the linear system for a throttle parameter value of 0.8

From Figure 7 and Figure 8, it is seen that all the eigenvalues of the linear systems obtained for the two throttle parameter values are on left half of the complex plane. Hence the linear systems are stable.

CHAPTER FIVE: UNCERTAINTY QUANTIFICAION VIA MONTE CARLO SIMULATION

Description of the Monte Carlo Simulation Performed

Because of a number of assumptions and simplifications, which have been made at different levels, the nominal model may not be an exact representation of the system. Secondly, the model reduction approximations also cause uncertainties in the model. Thirdly, the linearization causes uncertainties to the model due both to truncation of the Taylor series and the calculation of partial derivatives numerically. Furthermore, the parameters and coefficients used in the obtained nominal model are not perfectly known.

To find the uncertainty bounds on the nominal model, the Monte Carlo simulation is done for the system with some bounded random variation of some of the parameters. The mean model obtained from Monte Carlo simulations is used as the nominal model for the Mu Analysis.

The parametric uncertainties considered here are mainly on some of the structural properties which might vary slightly from the design value because of the manufacturing and installation processes. For example all the blades are not exactly the same. Different blades might have slightly different frequencies for bending and twist modes, and different damping ratios. Also a small uncertainty is considered in some of the geometry parameters, which may be caused by wear and tear etc.

Following are the structural properties in which uncertainties are considered with their nominal values:

Structural damping of bending mode, ς_b = 0.035

Frequency of pure bending mode, Q_b = 1.5

Structural damping of torsion mode, ς_t = 0.035

Frequency of pure torsion mode, Q_t = 3.3

The geometry parameters considered to have uncertainties and their nominal values are:

Position of the elastic axis of the blade from leading edge divided by blade-chord, ξ_{ea} = 0.55

Position of the center of gravity of the blade from leading edge divided by blade-chord, ξ_{cg} = 0.35

Position of the center of pressure of the blade from leading edge divided by blade-chord, ξ_{cp} = 0.35

The following empirical coefficients are also considered to have uncertainties:

Time scale for rotor loss, τ_r = 0.61

Time scale for stator loss, τ_s = 0.32

Coefficient of empirical rotor deviation function, δ_1 = 0.18

Coefficient of empirical rotor deviation function, $\delta_2 = 12^o$

Coefficient of empirical rotor loss function, L_{r1} = 1.8842

Coefficient of empirical rotor loss function, L_{r2} = - 0.5053

Coefficient of empirical rotor loss function, L_{r3} = 0.1219

Coefficient of empirical stator loss function, L_{s1} = 0.7429

Coefficient of empirical stator loss function, L_{s2} = - 0.1450

Coefficient of empirical stator loss function, L_{s3} = 0.0951

In the Monte Carlo simulations, each of the parameter is defined with a random variation about the nominal value within the uncertainty ranges described above. The linear model is

obtained in each iteration of the Monte Carlo simulation. A total of 1,000 iterations are used in the simulations to quantify the uncertainty bounds on the nominal model. The overall structure for the Monte Carlo simulations performed is presented below in Figure 9.

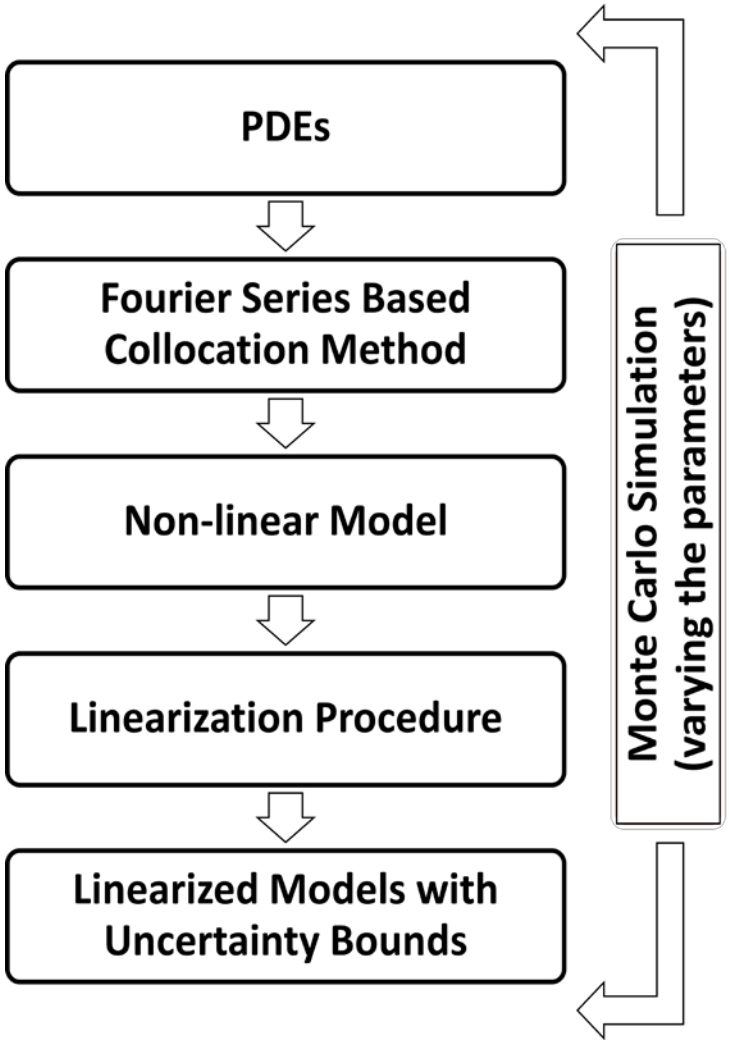

Figure 9: Overall structure for the Monte Carlo simulation

For obtaining a number of linear models and uncertainty bounds on the model, three different percentages of uncertainties are assumed on structural parameters-- 1%, 2.5% and 5% respectively. For all the cases considered in this thesis, the empirical coefficients are assumed to have 5% uncertainty about their nominal values while considering the state of the art

manufacturing processes that most often can obtain any geometry very accurately, the geometry parameters in the model are considered to have only 1% uncertainty.

Sample Results Obtained via Monte Carlo Simulation

The main purpose of performing a Monte Carlo simulation here is to quantify the uncertainty bounds on the linear model obtained in the previous step. A total of 1000 iterations of the Monte Carlo simulations were performed to obtain 1000 linear models for different combinations of the uncertain parameters. Based the linear models obtained, a mean model (i.e. nominal model) and the uncertainty bounds are calculated.

Analyzing the results obtained from the Monte Carlo simulation, it was found that the uncertainty bound on the linear model as well as the mean model is quite dependent on the percentage of uncertainty considered. For example, the original entry in the 22^{nd} column of the 22^{nd} row in the 22x22 system was -1.5625 for a throttle parameter value of 0.7. For an uncertainty of 1% on the structural parameters, the mean value of this entry for all 1000 iterations of Monte Carlo simulation was found to be -1.5628 with an uncertainty bound of 0.0195. On the other hand for an uncertainty of 5% on the structural parameters, the mean value of this entry for all 1000 iterations of Monte Carlo simulation was found to be -1.5665 with an uncertainty bound of 0.0781. Thus the results from the Monte Carlo simulation are in agreement with the natural expectation that the uncertainty bound on the linear model will be high when the percentage of uncertainty on the parameter values is high.

Liner stability analysis is also done for the linear models obtained via the Monte Carlo simulation. All the eigenvalues of 1000 iterations of the Monte Carlo simulation are shown in Figure 10 and a representative eigenvalue of the system as found in each iteration of the Monte Carlo simulation is presented in Figure 11. The eigenvalue plots shown here are for a Monte

Carlo simulation with considering a 5% uncertainty on the nominal values of the structural parameters, 1% uncertainty on the geometry parameters, and 5% uncertainty on the empirical coefficients in the model.

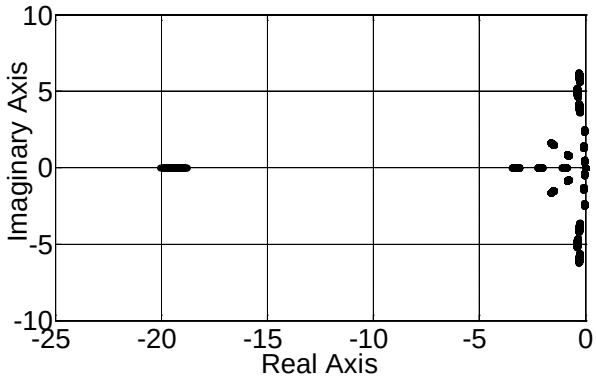

Figure 10: Eigenvalues of the system (all eigenvalues shown together)

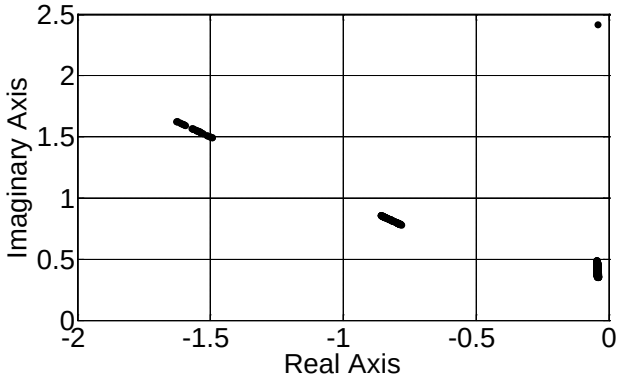

Figure 11: A representative eigenvalue of the system (for all iterations of Monte Carlo simulations)

From Figure 10 and Figure 11, it can be seen that all the eigenvalues of the system are in left half of the complex plane, which indicates a stable system for the uncertainty bounds used.

CHAPTER SIX: MU ANALYSIS AND SIMULATION RESULTS

Mu Analysis Procedure

In this section, the basic steps, in using the Mu analysis tool [24-29] to analyze the robust performance of the system in presence of parametric uncertainties in the system, are shown.

The linearized system obtained in chapter 5 can be written as:

$$\begin{aligned} \dot{X} &= [A]_{22\times 22} X + [B]_{22\times 22} u \\ y &= [I]_{22\times 22} X \end{aligned} \tag{52}$$

where B is a zero matrix because the system under analysis is open loop. The system output is the state. All the uncertainties in matrix A are modeled as additive parametric uncertainties as $A = (\hat{A} + W\Delta)$, where $\hat{A}$ is the mean value obtained in the Monte Carlo simulation, and $W = [W]_{22\times 22}$ contains the uncertainty boundary magnitude for each of the entries in matrix A. Δ is any kind of uncertainties with a magnitude upper bounded by 1.

The following are the basic steps involved in obtaining the synthesis model for the Mu analysis with the uncertainties accounted. The magnitudes of the uncertainty, their position in the main equation and their numbers are unique which vary with each equation. Let us use the first state equation as an example to show the basic approach.

$$\dot{X}_1 = \sum_{j=1}^{22} (A_{1,j} + W_{1,j}\Delta) X_j \tag{53}$$

Rewriting Eq. (53), the following equation is obtained.

$$\dot{X}_1 = \sum_{j=1}^{22} (A_{1,j} X_j + W_{1,j} X_j \Delta) \tag{54}$$

Let's define $W_{1,j} X_j = z_j$; Eq. (54) can then be written as:

$$\dot{X}_1 = \sum_{j=1}^{22} (A_{1,j} X_j + z_j \Delta) \tag{55}$$

Eq. (55) can be further written as

$$\dot{X}_1 = \sum_{j=1}^{22} A_{1,j} X_j + w_j \tag{56}$$

with the definition $z_j \Delta = w_j$.

Similarly, equations for the remaining 21 states are derived. For a particular throttle parameter value, the input and output relations derived for the open loop model is shown in Figure 12. In this model, there are 207 uncertainty signals input to the open loop system P from the uncertainty block Δ as shown in Figure 13. In the meantime, there are 207 signals $z_i, i = 1,...,207$ coming into the uncertainty block Δ from the open loop model P.

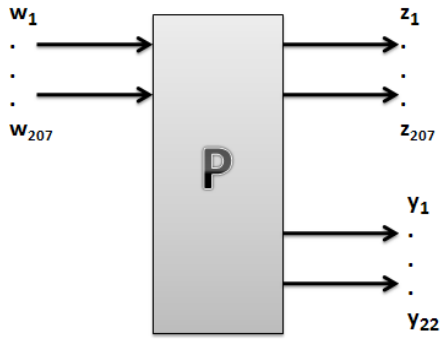

Figure 12: Open-loop model with the input/output relations

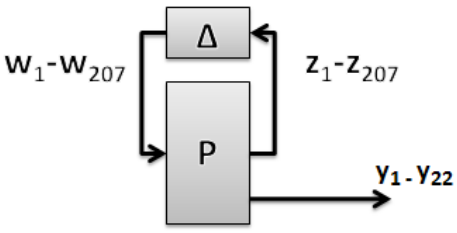

Figure 13: Synthesis model

The synthesized model is written in state space form as shown in Eq. (57) including states [**X**] $\in \mathbb{R}^{22x1}$, exogenous signals [**w**, **u**] $\in \mathbb{R}^{229x1}$, uncertainty input signals **z** $\in \mathbb{R}^{207x1}$ and output signals **y** $\in \mathbb{R}^{22x1}$

$$P = \begin{bmatrix} A_{22\times 22} & B_{22x229} \\ C_{229\times 22} & D_{229\times 229} \end{bmatrix} \tag{57}$$

Simulation Results

The structured singular value Mu from the Robust Control Toolbox in MATLAB® is used to analyze the robustness of the uncertain flutter model based on the synthesis model in Figure 14. As discussed in the previous section, for the particular throttle setting, the outputs of the synthesis system are composed of the output of the system and input to the uncertainty block. For calculating the robust performance, the frequency response of the system is calculated with the real uncertainty block specified. In this section the results of this analysis are discussed.

Three different cases with throttle parameter A_t = 0.7 are presented first here. Case I is a system with small uncertainty of 1% on all the parameters. The simulation result for this case is presented in Figure 14.

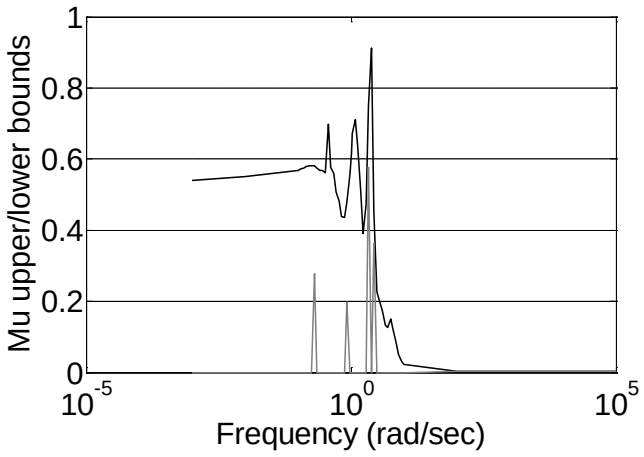

Figure 14: Robust analysis of case I flutter model

As can be seen in the Mu plot in Figure 14, the system is robustly stable to modeled uncertainty because the Mu value is less than one for all frequencies.

Case II is a system with an uncertainty of 2.5% in the parameter values. Simulation result for this case is presented in Figure 15. From Figure 15, it can be seen that this uncertain system is not robustly stable to the modeled uncertainty for certain frequencies. It can tolerate up to 30.9% of the modeled uncertainty and a destabilizing combination of 114% of the modeled uncertainty exists causing instability at 2.15 rad/s.

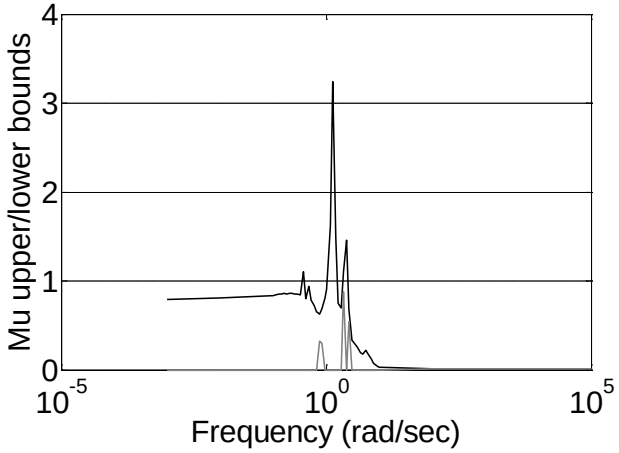

Figure 15: Robust analysis of case II flutter model

Case III involves a system with a relatively higher uncertainty of 5% on the structural parameters. It is shown in Figure 16 that the design is not robust with respect to the defined uncertainty. A destabilizing combination of 89.5% of the modeled uncertainty exists causing an instability at 2.73 rad/s. In addition to the stability conclusions obtained from the three cases we can get useful information about the frequency range the systems are stable within and the frequency that corresponds to the peak value of Mu.

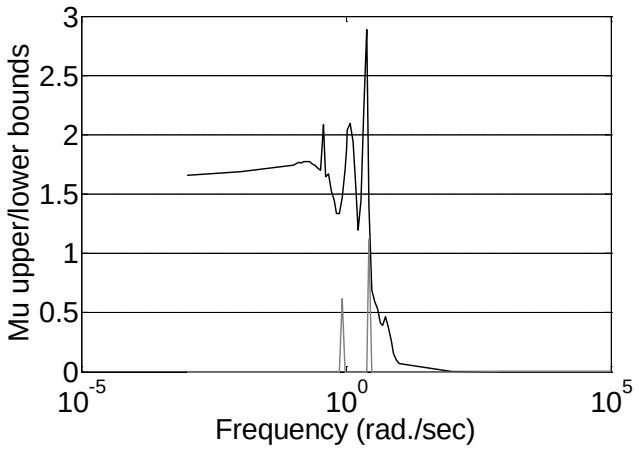

Figure 16: Robust analysis of case III flutter model

Mu analysis is then done on the system with 5% uncertainties on the structural parameters at two new operating points. The Mu plots for Case IV represented by throttle parameter A_t = 0.6, and Case V represented by A_t = 0.9 are shown in Figure 17 and Figure 18 respectively.

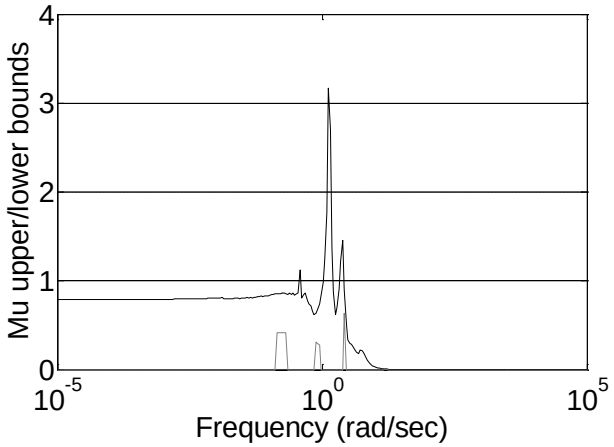

Figure 17: Robust analysis of case IV flutter model

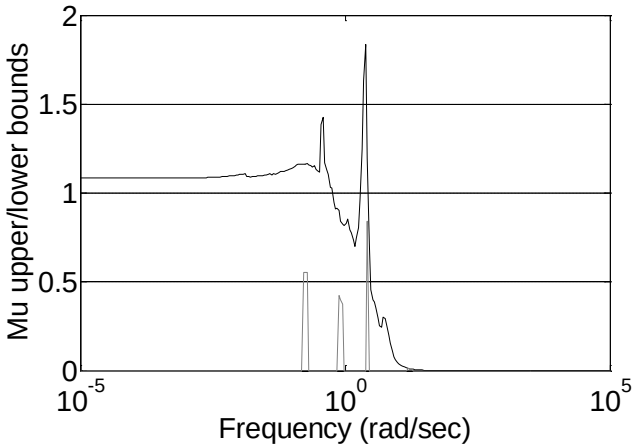

Figure 18: Robust analysis of case V flutter model

Looking at the Mu plot for Cases III, IV and Case V, which all have 5% uncertainty on structural parameters but different operating points, it is found that the frequency corresponding to the maximum value of Mu does not shift much depending on operating point. Hence a new set of values are assigned to the structural parameters to see if the frequency corresponding to the peak value of Mu would shift based on nominal values of the parameters. New values assigned for the structural properties are shown below:

Structural damping of bending mode, ς_b = 0.025

Frequency of pure bending mode, Q_b = 2.75

Structural damping of torsion mode, ς_t = 0.025

Frequency of pure torsion mode, Q_t = 5.5

The Mu plot for the new values of parameters with 5% uncertainty on structural parameters is shown in Figure 19.

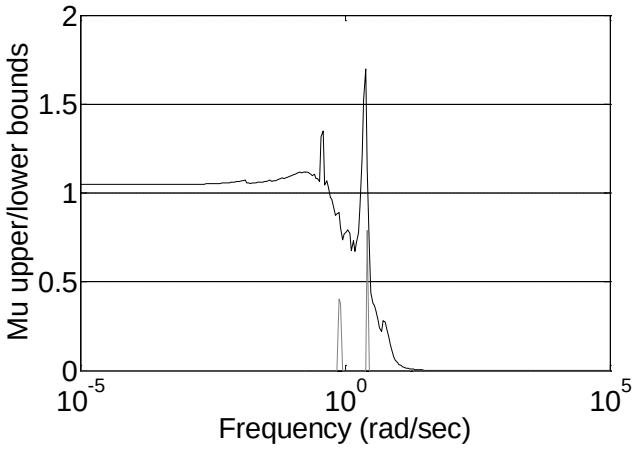

Figure 19: Robust analysis of case VI flutter model

As seen in Figure 19, like the previously stated cases with 5% uncertainties on the structural parameters, the system is not robustly stable for the modeled uncertainty. The peak frequency occurs at 2.42 rad/sec, which does not indicate a shift in frequency corresponding to instability based on changes in nominal value of structural parameters. Hence the linear models obtained for both cases were investigated and it was found that out of the 22 natural frequencies of the linear system, mainly the highest frequency are affected by the change in nominal values of structural parameters while the lower frequencies are not affected significantly. As a result the frequency corresponding to the peak value of Mu does not shift depending on nominal value of parameters, since it is the lower frequencies that are easily excited. Table 1 shows some higher and lower natural frequencies of the linear model obtained in Cases III and VI using different nominal values of structural parameters.

Table 1: Natural frequencies of linear models III and VI

Natural Frequency (rad/sec)	Case III Model	Case VI Model
High Frequencies	16.8	22.5
	5.93	5.94
	4.94	4.96
Low Frequencies	2.42	2.42
	2.21	2.21
	1.16	1.16

CHAPTER SEVEN: GENETIC ALGORITHM FOR FLUTTER PERFORMANCE OPTIMIZATION

In this chapter, the results obtained by applying Genetic Algorithm as an optimization tool are presented, along with a brief description of how the Genetic Algorithm works.

How the Algorithm Works

Genetic Algorithm is a global optimization tool, which is based on natural selection method. The algorithm first creates a random population and at the same time checks which set of the initial population matches best for as the solution to the optimization problem. The algorithm then creates new population in the new generation based on the fitness of the previous population. In the new generation, some of the set are chosen based on the best sets in previous iteration, which are called elite child. Also some populations are created by making random changes to the previous population. This is called mutation. Some other populations are created by combining the populations in the previous step. This is called crossover.

Results Obtained Using Genetic Algorithm

In this part of the thesis, Genetic Algorithm was applied to find the best parameter set in order to improve the damping characteristic of the system. One of the least damped modes was found to have a damping ratio of 0.0072, and this was improved to 0.008 by finding proper parameters via the Genetic Algorithm. This result demonstrates that the damping characteristics of the system can be improved by tuning the parameters using Genetic Algorithm. Table 2 shows the optimum parameter values as obtained by the Genetic Algorithm.

Table 2: Genetic Algorithm results

Parameter	Original Value(s)	Optimum Value(s)
Frequency for bending mode	1.5	1.4375
Frequency for twist mode	3.3	3.2195
Position of the elastic axis	0.55	0.5947
Position of the C.G.	0.35	0.34854
Position of the C.P.	0.35	0.3916
Damping ratio for bending	0.035	0.0304
Damping ratio for twist	0.035	0.0376
Empirical Coefficients for rotor deviation	0.61, 0.32	0.544, 0.231
Empirical Coefficients for rotor loss	1.8842, 0.5053, 0.1219	1.935, -0.573, 0.1219
Empirical Coefficients for stator loss	0.7429, 0.1450, 0.0951	0.6939, 0.05999, 0.09025

Presented in Figure 20 below is the iterative progress of the results in Genetic Algorithm.

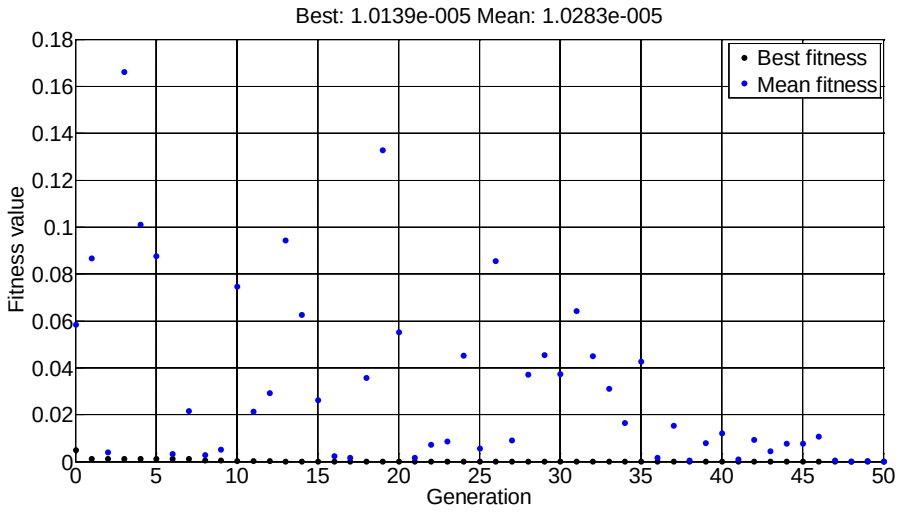

Figure 20: Genetic Algorithm iterations

CHAPTER EIGHT: SUMMARY AND CONCLUSION

In this thesis, the Mu tool is applied to analyze the robustness of a gas turbine compressor blade in terms of flutter. In this analysis, uncertainties, such as the ones arising from unmodeled dynamics, model order reduction, linearization, and imperfectly known parameters, are all considered. The nominal model and uncertainty bounds used in the Mu analysis are obtained via the Monte Carlo simulation based on a linearized model reduced from a publically available two dimensional, incompressible flow model coupled with structural dynamics. Consideration of uncertainty on the empirical coefficients in the model essentially accounts for the modeling error.

To do an accurate robust performance analysis using Mu tool, a model that can capture the physical phenomenon approximately is necessary. The Mu tool can make strong claim about robustness by utilizing a well developed mathematical framework. However, it can give very accurate results, if the robustness analysis with respect to parametric uncertainties is done based on a nearly-accurate model. In case of absence of an accurate model, the uncertainty bound on the nominal model would be high and a design using Mu tool could be too conservative. With a high accuracy model and the steps shown in this thesis, the robust performance of the compressor blades can be determined accurately and used by designers to predict safe operation conditions such that unstable operation regions can be avoided.

Future works will include validation of the results using the experimental results found in open literature. The physical phenomenon of flutter being very complicated, it is often very difficult to accurately capture the relevant system dynamics in a mathematical model, and hence a robust controller is highly desirable to ensure satisfactory performance under the presence of uncertainty due to inaccurate model. The future endeavor of this research would include development of a robust controller for suppressing flutter in turbomachinery.

APPENDIX: EQUATIONS USED IN COLLOCATION METHOD

The following time-derivatives are then derived based on the approximation made in Eq. (42) to (46):

$$\frac{\partial \alpha}{\partial \mathrm{t}} = \frac{\partial a_0(\mathrm{t})}{\partial \mathrm{t}} + \frac{\partial a_1(\mathrm{t})}{\partial \mathrm{t}}\cos(\theta) + \frac{\partial \hat{a}_1(\mathrm{t})}{\partial \mathrm{t}}\sin(\theta) \tag{58}$$

$$\frac{\partial q}{\partial \mathrm{t}} = \frac{\partial b_0(\mathrm{t})}{\partial \mathrm{t}} + \frac{\partial b_1(\mathrm{t})}{\partial \mathrm{t}}\cos(\theta) + \frac{\partial \hat{b}_1(\mathrm{t})}{\partial \mathrm{t}}\sin(\theta) \tag{59}$$

$$\frac{\partial^2 \alpha}{\partial \mathrm{t}^2} = \frac{\partial^2 a_0(\mathrm{t})}{\partial \mathrm{t}^2} + \frac{\partial^2 a_1(\mathrm{t})}{\partial \mathrm{t}^2}\cos(\theta) + \frac{\partial^2 \hat{a}_1(\mathrm{t})}{\partial \mathrm{t}^2}\sin(\theta) \tag{60}$$

$$\frac{\partial^2 q}{\partial \mathrm{t}^2} = \frac{\partial^2 b_0(\mathrm{t})}{\partial \mathrm{t}^2} + \frac{\partial^2 b_1(\mathrm{t})}{\partial \mathrm{t}^2}\cos(\theta) + \frac{\partial^2 \hat{b}_1(\mathrm{t})}{\partial \mathrm{t}^2}\sin(\theta) \tag{61}$$

The spatial-derivatives are then derived:

$$\frac{\partial \alpha}{\partial \theta} = -a_1(\mathrm{t})\sin(\theta) + \hat{a}_1(\mathrm{t})\cos(\theta) \tag{62}$$

$$\frac{\partial q}{\partial \theta} = -b_1(\mathrm{t})\sin(\theta) + \hat{b}_1(\mathrm{t})\cos(\theta) \tag{63}$$

$$\frac{\partial^2 \alpha}{\partial \theta^2} = -a_1(\mathrm{t})\cos(\theta) - \hat{a}_1(\mathrm{t})\sin(\theta) \tag{64}$$

$$\frac{\partial^2 q}{\partial \theta^2} = -b_1(\mathrm{t})\cos(\theta) - \hat{b}_1(\mathrm{t})\sin(2\theta) \tag{65}$$

The mixed derivatives are found as follows:

$$\frac{\partial^2 \alpha}{\partial t \partial \theta} = -\frac{\partial a_1(\mathrm{t})}{\partial \mathrm{t}}\sin(\theta) + \frac{\partial \hat{a}_1(\mathrm{t})}{\partial \mathrm{t}}\cos(\theta) \tag{66}$$

$$\frac{\partial^2 q}{\partial t \partial \theta} = -\frac{\partial b_1(\mathrm{t})}{\partial \mathrm{t}}\sin(\theta) + \frac{\partial \hat{b}_1(\mathrm{t})}{\partial \mathrm{t}}\cos(\theta) \tag{67}$$

$$\frac{\partial}{\partial t}\left(\frac{\partial^2 \alpha}{\partial t \partial \theta}\right) = -\frac{\partial^2 a_1(\mathrm{t})}{\partial \mathrm{t}^2}\sin(\theta) + \frac{\partial^2 \hat{a}_1(\mathrm{t})}{\partial \mathrm{t}^2}\cos(\theta) \tag{68}$$

$$\frac{\partial}{\partial t}\left(\frac{\partial^2 q}{\partial t \partial \theta}\right) = -\frac{\partial^2 b_1(\mathrm{t})}{\partial \mathrm{t}^2}\sin(\theta) + \frac{\partial^2 \hat{b}_1(\mathrm{t})}{\partial \mathrm{t}^2}\cos(\theta) \tag{69}$$

$$\frac{\partial}{\partial t}\left(\frac{\partial^2 \alpha}{\partial \theta^2}\right) = -\frac{\partial a_1(\mathrm{t})}{\partial \mathrm{t}}\cos(\theta) - \frac{\partial \hat{a}_1(\mathrm{t})}{\partial \mathrm{t}}\sin(\theta) \tag{70}$$

$$\frac{\partial}{\partial t}\left(\frac{\partial^2 q}{\partial \theta^2}\right) = -\frac{\partial b_1(\mathrm{t})}{\partial \mathrm{t}}\cos(\theta) - \frac{\partial \hat{b}_1(\mathrm{t})}{\partial \mathrm{t}}\sin(\theta) \tag{71}$$

Based on the above coordinates shown in Eq. (15) to Eq. (18), the following derivates are found:

$$\frac{\partial x_{le}}{\partial \theta} = -\sin(\gamma_r)\frac{\partial q}{\partial \theta} - \xi_{ea} c \sin(\gamma_r - \alpha)\frac{\partial \alpha}{\partial \theta} \tag{72}$$

$$\frac{\partial x_{le}}{\partial t} = -\sin(\gamma_r)\frac{\partial q}{\partial t} - \xi_{ea} c \sin(\gamma_r - \alpha)\frac{\partial \alpha}{\partial t} \tag{73}$$

$$\frac{\partial^2 x_{le}}{\partial \theta^2} = -\sin(\gamma_r)\frac{\partial^2 q}{\partial \theta^2} - \xi_{ea} c \left\{\cos(\gamma_r - \alpha)\left(-\frac{\partial \alpha}{\partial \theta}\right)\left(\frac{\partial \alpha}{\partial \theta}\right) + \sin(\gamma_r - \alpha)\left(\frac{\partial^2 \alpha}{\partial \theta^2}\right)\right\} \tag{74}$$

$$\frac{\partial^2 x_{le}}{\partial t^2} = -\sin(\gamma_r)\frac{\partial^2 q}{\partial t^2} - \xi_{ea} c \left\{\cos(\gamma_r - \alpha)\left(-\frac{\partial \alpha}{\partial t}\right)\left(\frac{\partial \alpha}{\partial t}\right) + \sin(\gamma_r - \alpha)\left(\frac{\partial^2 \alpha}{\partial t^2}\right)\right\} \tag{75}$$

$$\frac{\partial^2 x_{le}}{\partial t \partial \theta} = -\sin(\gamma_r)\frac{\partial^2 q}{\partial t \partial \theta} - \xi_{ea} c \left\{\cos(\gamma_r - \alpha)\left(-\frac{\partial \alpha}{\partial t}\right)\left(\frac{\partial \alpha}{\partial \theta}\right) + \sin(\gamma_r - \alpha)\left(\frac{\partial^2 \alpha}{\partial t \partial \theta}\right)\right\} \tag{76}$$

$$\frac{\partial x_{te}}{\partial \theta} = -\sin(\gamma_r)\frac{\partial q}{\partial \theta} + (1 - \xi_{ea}) c \sin(\gamma_r - \alpha)\frac{\partial \alpha}{\partial \theta} \tag{77}$$

$$\frac{\partial x_{te}}{\partial t} = -\sin(\gamma_r)\frac{\partial q}{\partial t} + (1 - \xi_{ea}) c \sin(\gamma_r - \alpha)\frac{\partial \alpha}{\partial t} \tag{78}$$

$$\frac{\partial^2 x_{te}}{\partial \theta^2} = -\sin(\gamma_r)\frac{\partial^2 q}{\partial \theta^2} + (1 - \xi_{ea}) c \left\{\cos(\gamma_r - \alpha)\left(-\frac{\partial \alpha}{\partial \theta}\right)\left(\frac{\partial \alpha}{\partial \theta}\right) + \sin(\gamma_r - \alpha)\left(\frac{\partial^2 \alpha}{\partial \theta^2}\right)\right\} \tag{79}$$

$$\frac{\partial^2 x_{te}}{\partial t^2} = -\sin(\gamma_r)\frac{\partial^2 q}{\partial t^2} + (1-\xi_{ea})c\left\{\cos(\gamma_r-\alpha)\left(-\frac{\partial\alpha}{\partial t}\right)\left(\frac{\partial\alpha}{\partial t}\right) + \sin(\gamma_r-\alpha)\left(\frac{\partial^2\alpha}{\partial t^2}\right)\right\} \quad (80)$$

$$\frac{\partial^2 x_{te}}{\partial t\partial\theta} = -\sin(\gamma_r)\frac{\partial^2 q}{\partial t\partial\theta} + (1-\xi_{ea})c\left\{\cos(\gamma_r-\alpha)\left(-\frac{\partial\alpha}{\partial t}\right)\left(\frac{\partial\alpha}{\partial\theta}\right) + \sin(\gamma_r-\alpha)\left(\frac{\partial^2\alpha}{\partial t\partial\theta}\right)\right\} \quad (81)$$

$$\frac{\partial\theta_{le}}{\partial\theta} = 1+\cos(\gamma_r)\frac{\partial q}{\partial\theta} + \xi_{ea}c\cos(\gamma_r-\alpha)\frac{\partial\alpha}{\partial\theta} \quad (82)$$

$$\frac{\partial\theta_{le}}{\partial t} = \cos(\gamma_r)\frac{\partial q}{\partial t} + \xi_{ea}c\cos(\gamma_r-\alpha)\frac{\partial\alpha}{\partial t} \quad (83)$$

$$\frac{\partial^2\theta_{le}}{\partial\theta^2} = \cos(\gamma_r)\frac{\partial^2 q}{\partial\theta^2} + \xi_{ea}c\left\{\sin(\gamma_r-\alpha)\left(\frac{\partial\alpha}{\partial\theta}\right)\left(\frac{\partial\alpha}{\partial\theta}\right) + \cos(\gamma_r-\alpha)\left(\frac{\partial^2\alpha}{\partial\theta^2}\right)\right\} \quad (84)$$

$$\frac{\partial^2\theta_{le}}{\partial t^2} = \cos(\gamma_r)\frac{\partial^2 q}{\partial t^2} + \xi_{ea}c\left\{\sin(\gamma_r-\alpha)\left(\frac{\partial\alpha}{\partial t}\right)\left(\frac{\partial\alpha}{\partial t}\right) + \cos(\gamma_r-\alpha)\left(\frac{\partial^2\alpha}{\partial t^2}\right)\right\} \quad (85)$$

$$\frac{\partial^2\theta_{le}}{\partial t\partial\theta} = \cos(\gamma_r)\frac{\partial^2 q}{\partial t\partial\theta} + \xi_{ea}c\left\{\sin(\gamma_r-\alpha)\left(\frac{\partial\alpha}{\partial t}\right)\left(\frac{\partial\alpha}{\partial\theta}\right) + \cos(\gamma_r-\alpha)\left(\frac{\partial^2\alpha}{\partial t\partial\theta}\right)\right\} \quad (86)$$

$$\frac{\partial\theta_{te}}{\partial\theta} = 1+\cos(\gamma_r)\frac{\partial q}{\partial\theta} - (1-\xi_{ea})c\cos(\gamma_r-\alpha)\frac{\partial\alpha}{\partial\theta} \quad (87)$$

$$\frac{\partial\theta_{te}}{\partial t} = \cos(\gamma_r)\frac{\partial q}{\partial t} - (1-\xi_{ea})c\cos(\gamma_r-\alpha)\frac{\partial\alpha}{\partial t} \quad (88)$$

$$\frac{\partial^2\theta_{te}}{\partial\theta^2} = \cos(\gamma_r)\frac{\partial^2 q}{\partial\theta^2} - (1-\xi_{ea})c\left\{\sin(\gamma_r-\alpha)\left(\frac{\partial\alpha}{\partial\theta}\right)\left(\frac{\partial\alpha}{\partial\theta}\right) + \cos(\gamma_r-\alpha)\left(\frac{\partial^2\alpha}{\partial\theta^2}\right)\right\} \quad (89)$$

$$\frac{\partial^2\theta_{te}}{\partial t^2} = \cos(\gamma_r)\frac{\partial^2 q}{\partial t^2} - (1-\xi_{ea})c\left\{\sin(\gamma_r-\alpha)\left(\frac{\partial\alpha}{\partial t}\right)\left(\frac{\partial\alpha}{\partial t}\right) + \cos(\gamma_r-\alpha)\left(\frac{\partial^2\alpha}{\partial t^2}\right)\right\} \quad (90)$$

$$\frac{\partial^2\theta_{te}}{\partial t\partial\theta} = \cos(\gamma_r)\frac{\partial^2 q}{\partial t\partial\theta} - (1-\xi_{ea})c\left\{\sin(\gamma_r-\alpha)\left(\frac{\partial\alpha}{\partial t}\right)\left(\frac{\partial\alpha}{\partial\theta}\right) + \cos(\gamma_r-\alpha)\left(\frac{\partial^2\alpha}{\partial t\partial\theta}\right)\right\} \quad (91)$$

Following derivatives of the path lengths, as shown in Eq. (13) and Eq. (14) are then found:

$$\frac{\partial^2 s_{le}}{\partial t \partial \theta} = \frac{\left(\frac{\partial x_{le}}{\partial \theta}\right)\left(\frac{\partial^2 x_{le}}{\partial t \partial \theta}\right) + \left(\frac{\partial \theta_{le}}{\partial \theta}\right)\left(\frac{\partial^2 \theta_{le}}{\partial t \partial \theta}\right)}{\sqrt{\left(\frac{\partial x_{le}}{\partial \theta}\right)^2 + \left(\frac{\partial \theta_{le}}{\partial \theta}\right)^2}} \tag{92}$$

$$\frac{\partial^2 s_{le}}{\partial \theta^2} = \frac{\left(\frac{\partial x_{le}}{\partial \theta}\right)\left(\frac{\partial^2 x_{le}}{\partial \theta^2}\right) + \left(\frac{\partial \theta_{le}}{\partial \theta}\right)\left(\frac{\partial^2 \theta_{le}}{\partial \theta^2}\right)}{\sqrt{\left(\frac{\partial x_{le}}{\partial \theta}\right)^2 + \left(\frac{\partial \theta_{le}}{\partial \theta}\right)^2}} \tag{93}$$

$$\frac{\partial^2 s_{te}}{\partial t \partial \theta} = \frac{\left(\frac{\partial x_{te}}{\partial \theta}\right)\left(\frac{\partial^2 x_{te}}{\partial t \partial \theta}\right) + \left(\frac{\partial \theta_{te}}{\partial \theta}\right)\left(\frac{\partial^2 \theta_{te}}{\partial t \partial \theta}\right)}{\sqrt{\left(\frac{\partial x_{te}}{\partial \theta}\right)^2 + \left(\frac{\partial \theta_{te}}{\partial \theta}\right)^2}} \tag{94}$$

$$\frac{\partial^2 s_{te}}{\partial \theta^2} = \frac{\left(\frac{\partial x_{te}}{\partial \theta}\right)\left(\frac{\partial^2 x_{te}}{\partial \theta^2}\right) + \left(\frac{\partial \theta_{te}}{\partial \theta}\right)\left(\frac{\partial^2 \theta_{te}}{\partial \theta^2}\right)}{\sqrt{\left(\frac{\partial x_{te}}{\partial \theta}\right)^2 + \left(\frac{\partial \theta_{te}}{\partial \theta}\right)^2}} \tag{95}$$

Partial derivates related to the control volume deformation are then found as follows:

$$\frac{\partial^2 V}{\partial t \partial \theta} = \frac{c}{2}\left[\cos(\gamma_r - \alpha)\left(\frac{\partial^2 s_{le}}{\partial t \partial \theta} + \frac{\partial^2 s_{te}}{\partial t \partial \theta}\right) + \left(\frac{\partial s_{le}}{\partial \theta} + \frac{\partial s_{te}}{\partial \theta}\right)\sin(\gamma_r - \alpha)\left(\frac{\partial \alpha}{\partial t}\right)\right] \tag{96}$$

$$\frac{\partial^2 V}{\partial \theta^2} = \frac{c}{2}\left[\cos(\gamma_r - \alpha)\left(\frac{\partial^2 s_{le}}{\partial \theta^2} + \frac{\partial^2 s_{te}}{\partial \theta^2}\right) + \left(\frac{\partial s_{le}}{\partial \theta} + \frac{\partial s_{te}}{\partial \theta}\right)\sin(\gamma_r - \alpha)\left(\frac{\partial \alpha}{\partial \theta}\right)\right] \tag{97}$$

LIST OF REFERENCES

[1] de Jager, B. "Rotating Stall and Surge Control: A Survey," *Proceedings of the 35th Conference on Decision and Control,* New Orleans, LA, 1995, pp. 1857-1862.

[2] Emmons, H.W., Pearson, C.E. and Grant, H.P. "Compressor Surge and Stall," *Transactions of the ASME,* 77, 1955, pp. 455-469.

[3] Horlock, J.H., *Axial Flow Compressors: Fluid Mechanics and Thermodynamics*, Butterworths Scientific Publications, London.

[4] El-Aini, Y., deLaneuville, R., Stoner, A., and Capece, V., "High Cycle Fatigue of Turbomachinery Components-- Industry Perspective," *AIAA paper 97-3365*.

[5] Rice, T., Bell, D., Singh, G., "Identification of the Stability Margin between Safe Operation and the Onset of Blade Flutter," *Proceedings of ASME Turbo Expo 2007: Power for Land, Sea and Air,* Montreal, Canada, May 14-17, 2007.

[6] Khalak, A., "A Framework for Flutter Clearance of Aeroengine Blades," *Proceedings of the ASME Turbo Expo 2001*, New Orleans, Louisiana, June 4-7, 2001.

[7] Epureanu, B.I., "A Parametric Analysis of Reduced Order Models of Viscous Flows in Turbomachinery," *Journal of Fluids and Structures*, 17, 2033, pp 971-982.

[8] Wong, M.T.M., "System Modeling and Control Studies of Flutter in Turbomachinery", *MS Thesis,* Massachusetts Institute of Technology, 1997.

[9] Copeland, G.S., and Rey, G., "Non-linear Modeling, Analysis and Control of

Turbomachinery Stall Flutter," *Air Force Office of Scientific Research Contract Report,* AFRL-SR-BL-TR-98-0694, 1998.

[10] Gysling, D.L. and Myers, M.R., "A framework for analyzing the dynamics of Flexibly-Bladed Turbomachines," *ASME 96-GT-440, Intl Gas Turbine and Aeroengine Congress and Exhibition,* Birmingham, U.K., June 10-13, 1996

[11] Longley, J.P., "A Review of Nonsteady Flow Models for Compressor Stability," *Journal of Turbomachinery,* Vol. 116, April 1994, pp. 202-215.

[12] Moore, F.K., Greitzer, E.M., "A Theory of Post Stall Transients in Axial Compression Systems: Part I and II," *ASME Journal of Engineering for Gas Turbine and Power,* Vol. 108, 1986, pp 68-76.

[13] Adamczyk, J. J. et al, "Supersonic Stall Flutter of High Speed fans," *Journal of Engineering for Power,* Vol. 104, 1982, pp. 675-682.

[14] Adamczyk, J. J., "Analysis of Supersonic Stall Bending Flutter in Axial Flow Compressor by Actuator Disk Theory," *NASA technical Paper 1345,* Nov 1978.

[15] Dowell, et al. A Modern Course in Aeroelasticity, Sijthoff and Noordhoff, Alphen aan den Rijn, The Netherlands, 1978.

[16] Zaeit, C., Akhrif, O., Saydy, L., "Modeling and Non-linear Control of a Gas Turbine," *Proceedings of IEEE International Symposium on Industrial Electronics*, Montreal, Quebec, Canada, July 9-12, 2006.

[17] Boyd, J.P., *Chebyshev and Fourier Spectral Methods*, New York, Dover Publications Inc., 2000.

[18] Bell, D.L., and He, L., "Three Dimensional Unsteady Flow for an Oscillating Turbine Blade and the Influence of Tip Leakage," *ASME Journal of Turbomachinery*, Vol. 122, No. 1, 2000, pp 93-101.

[19] Bölcs, A., Fransson, T.H., "Aeroelasticity in Turbomachine: Comparison of Theoretical and Experimental Cascade Results," *Communication du Laboratoire de Thermiqe Thermique Appliquée et de Turbomachines*, 1986, No. 13, Lusuanne, EPFL.

[20] Boyce, P. M., *Gas Turbine Engineering Handbook*, 3rd Ed., Burlington MA, Elsevier Inc., 2006, pp. 310-311.

[21] Carta, F.O, and St. Hilaire, A.O., "Effects of Interblade Phase Angle on Cascade Pitching Stability," *ASME Journal of Engineering for Power*, Vol. 102, 1980, pp. 391-396

[22] Whitehead, D. S., "Vibration of Cascade Blades Treated by Actuator Disk Methods," *Proceedings of the Institute of Mechanical Engineers*, Vol. 173, no. 21, pp. 555-574.

[23] Shubov, M. A., "Mathematical Modeling and Analysis of Flutter in Bending-Torsion Coupled Beams, Rotating Blades, and Hard Disk Drives," *Journal of Aerospace Engineering*, Vol. 17, No. 2, April 1, 2004

[24] Balas, G. J., Doyle, J. C., Glover, K., Packard, A., and Smith, R., *μ-Analysis and Synthesis Toolbox: User's Guide*. The Mathworks Inc., 1991.

[25] Balas, G., Chiang, R., Packard, A., and Sofonov, M., *Robust Control Toolbox: User's Guide*. Natick, MA: MathWorks, 2005.

[26] Hoekstra, D., "QFT robust control design and MU analysis for a solar orbital transfer vehicle," The Netherlands, Technische Universiteit Eindhoven, 2004.

[27] Lind, R., and Brenner, M., "Flutterometer: An On-Line Tool to Predict Robust Flutter Margins," *Journal of Aircraft*, Vol. 37, No. 6, 2000, pp. 1105–1112.

[28] Micklow, J and Jeffers, J., "Semi-Actuator Disk Theory for Compressor Choke Flutter," *NASA Contract Report NAS3-20060*, Oct 1980

[29] Xu, Y., Fitz-Coy, N., Lind, R., and Tatsch4, A., "μ Control for Satellites Formation Flying," *Journal of Aerospace Engineering*, Vol. 20, 2007, pp. 10–21.

[30] Xu, Y., Suman, S., "Robust Stationkeeping Control for Libration Point Quasi-Periodic Orbits," *Journal of Aerospace Engineering*, Vol. 21, No. 2, April 1, 2008, pp. 102–115.

[31] Back, T., "Evolutionary Algorithms in Theory and Practice," *Oxford University Press*, 1996.

[32] Charbonneu, P., "An Introduction to Genetic Algorithm for Numerical Optimization," *Technical Note, National Center for Atmospheric Research*, March 2002.